Tuning work function difference of copper/cobalt oxides heterointerfaces enables efficient electrochemical nitrate reduction

Chao Feng [a,b,1], Weiliang Zhou [a,1], Hanyang Wu [a], Qihua Huo [a], Jiaxin Shao [a], Xuan Li [a], Hengpan Yang [a], Qi Hu [a,*], Chuanxin He [a]

[a] College of Chemistry and Environmental Engineering, Shenzhen University, Shenzhen, Guangdong 518060, People's Republic of China
[b] Institute of Microscale Optoelectronics, Shenzhen University, Shenzhen 518060, Guangdong, People's Republic of China

ABSTRACT

Metal/metal-oxide heterointerfaces receive extensive attention in electrocatalysis on account of the strong synergy between the two components at the interface. However, the key factor governing such interfacial synergy is still unclear, making it extremely challenging to rationally design electrocatalyst with desired heterointerfaces. Here, we select metallic copper/cobalt-oxide (i.e., Cu/Co_3O_4) heterointerfaces as model catalysts for the nitrate reduction reaction (NO_3RR) and tuned work function difference ($\Delta\Phi$) between Cu/Co_3O_4 by introducing oxygen vacancies (O_v) on Co_3O_4. By combing experimental and theoretic results, we observe that the $\Delta\Phi$ is a key factor that governs the interfacial synergy, which included the transfer of electrons from Cu to Co_3O_4 and the spillover of hydrogen from Co_3O_4 to Cu. Consequently, the Cu/Co_3O_4 interface with an optimized $\Delta\Phi$ displayed the best NO_3^-RR performance, outperforming most of other reported electrocatalysts. The above findings will create new opportunities for rationally designing heterointerfaces for efficient electrocatalysis by tuning $\Delta\Phi$.

1. Introduction

The creation of heterointerfaces, such as metal/metal-oxide interfaces, has gained considerable recognition as an effective approach to adjust the selectivity and activity of electrocatalysts for different reactions. This is attributed to the synergistic effect of the two components at the heterointerfaces, resulting in enhanced performance [1–3]. Generally, the synergistic effect originates from the spontaneous electron transfer at heterointerfaces, which consequently regulates the electronic structure of active sites and reduces the energy barrier of electrocatalytic reactions [4–8]. Moreover, various catalyst engineering strategies, including crystal facet/phase control [9–11], defect structure introduction [12–15], and heteroatom doping [16–20], have been developed to tune interfacial electron transfer and further enhance electrocatalytic performance. Despite the vigorous efforts made to optimize the synergistic effect of heterointerfaces [21–23], the mechanism of interfacial electron transfer remains elusive and not yet fully understood, making it challenging to precisely control the direction and degree of such electron transfer. Therefore, understanding the mechanism of interfacial electron transfer and identifying the key factors

controlling such transfer are necessary for rationally designing advanced heterointerfaces.

In heterogeneous structures, the Fermi energy-level difference between two phases can greatly affect the interfacial charge transfer process [22,24]. Typically, in metal/metal-oxide heterogeneous interfacial structures, when there is a small difference in Fermi energy levels between the two phases, the interfacial charge transfer is hindered, and the accumulated charge at the interface gradually decreases, which can significantly reduce the energy barrier of interfacial hydrogen spillover [25,26]. It has been established that *H plays an active role in promoting most proton-coupled electron reactions [27–29]. Similarly, the $\Delta\Phi$ of heterogeneous structural materials plays a major role in adjusting the heterogeneous interfacial reaction energy barrier since it is easily adjustable [30]. Based on the strong correlation between $\Delta\Phi$ and the Fermi energy level, we hypothesize that the variation in $\Delta\Phi$ between metal and metal oxides plays a key role in interfacial hydrogen spillover kinetics and interfacial electronic structural changes. It is speculated that a small $\Delta\Phi$ can substantially reduce the hydrogen spillover barrier and decrease the interfacial charge accumulation, thus providing more active hydrogen (*H). This *H, in combination with the synergistic effect

---

of the active sites, can substantially improve the electrocatalytic reduction performance of the catalyst. If this assumption holds true, a simple examination of the $\Delta\Phi$ between two components in a heterogeneous interfacial structure, can be beneficial for the design and development of catalysts involving interfacial hydrogen transfer.

Herein, we selected a nitrate reduction reaction (NO_3^-RR) involving a complex nine-proton-coupled eight-electron transfer process as the model reaction [31–34]. The aim is to determine the key factor that regulates the process of interfacial electron transfer and the NO_3^-RR by controllably creating several Cu/Co_3O_4 heterointerfaces with different O_v concentrations. The results indicated that $\Delta\Phi$ played a crucial role in controlling *H overflow and interfacial charge transfer. The experimental results and density functional theory (DFT) calculations further confirmed that a suitable $\Delta\Phi$ between the heterogeneous interfacial structures can optimize the electronic structure of the two phases, the main expression the transfer of electrons from Cu to Co_3O_4 and the spillover of hydrogen from Co_3O_4 to Cu. It can effectively enhance the synergistic effect of the heterogeneous interface and improve the catalytic activity. Cu in Cu/CoO_x @NFs model catalysts acted as the active site for direct electrocatalytic reduction reaction and exhibited strong catalytic activity and adsorption properties for the reactants. CoO_x with a moderate O_v concentration served as the main active site for water dissociation and *H generation. The amount of generated *H that overflowed onto the Cu surface significantly increased the degree of hydrogen coverage on the Cu surface, which in turn promoted the NO_3^-RR. As result, at a small potential of -0.15 V vs. reversible hydrogen electrode (RHE), the Faradaic efficiency (FE) of NH_3 (FE_{NH_3}) production was up to 95.1%, and the current density was as high as 400 mA cm^{-2}. This work may provide deep insights into mechanism of metal/metal-oxide heterointerfaces for the efficient electrocatalytic reduction.

2. Experimental sections

2.1. Materials

All of the chemical reagents used in this study were purchased from Aladdin (analytical grade). All chemicals were directly utilized without further purification.

2.2. Catalyst preparation

2.2.1. The synthesis procedure of the CuCo-based precursor was as follows

2.2.1.1. Synthesis of CuCo-PBAs. Copper-cobalt Prussian blue analogs (CuCo-PBAs) cubes were synthesized by a simple room temperature co-precipitation method with reference to the method in the literature [35]. Specifically, 102.3 mg of copper chloride (CuCl$_2$·2 H$_2$O) and 117.6 mg of sodium citrate dihydrate (Na$_3$C$_6$H$_5$O$_7$·2 H$_2$O) were mixed and dissolved in 20 ml deionized water until the solution was clarified, denoted as solution A. Another clear solution B was prepared, namely, 132.9 mg of potassium cobalt cyanide (K$_3$[Co(CN)$_6$]) was dissolved in 20 ml of deionized water with stirring. At room temperature, liquid B was quickly poured into liquid A, magnetically stirred for 3 min, then placed in an ultrasonic water bath for 3 min, left to age overnight. The precipitate was collected, washed with water and ethanol centrifugation, and dried at 60 °C for 12 h to obtain a blue color CuCo-PBAs.

2.2.1.2. Synthesis of CoCo-PBAs. Replace copper chloride (CuCl$_2$·2 H$_2$O) with cobalt chloride (CoCl$_2$·6 H$_2$O) of the same molar mass, and synthesize it according to the above method to obtain pink CoCo-PBAs.

2.2.1.3. Synthesis of Cu$_1$Co$_{0.5}$-PBAs. Change the amount of potassium cobalt cyanide (i.e. the amount of cobalt element) added during the synthesis of CuCo-PBAs, half of its mass, and keep the rest of the steps

unchanged, and the synthesis was denoted as Cu$_1$Co$_{0.5}$-PBAs.

2.2.1.4. Synthesis of Cu$_{0.5}$Co$_1$-PBAs. Change the amount of copper chloride (i.e. the amount of copper element) added during the synthesis of CuCo-PBAs, half of its mass, and keep the rest of the steps unchanged, and the synthesized product was denoted as Cu$_{0.5}$Co$_1$-PBAs.

2.2.2. The synthesis procedure of the active catalyst and its comparative samples were as follows

2.2.2.1. Preparation of active catalyst Cu/CoO$_x$ @NFs. The pre-catalyst CuO/Co$_3$O$_4$ @NFs was prepared by combining the electrospinning process with the high temperature pyrolysis technique using the synthesized CuCo-PBAs as the precursor. Specific, 1.0 g of polyacrylonitrile (PAN, Mw=150000 g mol^{-1}) was added to 14 ml of N, N-dimethylformamide (DMF) solvent and stirred under sealed and dry conditions until the solution was homogeneous, then add 1.0 g CuCo-PBA and stir magnetically at room temperature to form an electrospinning solution. The above electrospinning solution was injected into a 20 ml spinning syringe, and the electrospinning was carried out at a pushing speed of 1 ml h^{-1}, a spinning voltage of 18 kV, and a constant temperature and dry atmosphere (CuCo-PBA@PAN). The collected nanofiber membranes were dried in vacuum for 12 h, and then pre-oxidized in air at 280 °C for 3 h to further stabilize the nanofiber structure. Then, the PAN was removed from the fibers by calcining at a heating rate of 1 °C min^{-1} in a high temperature muffle furnace at 500 °C for 2 h, and the product was denoted as CuO/Co$_3$O$_4$ @NFs. Finally, CuO/Co$_3$O$_4$ @NFs was reconstituted at 300 °C in a mixed Ar/H$_2$ reducing atmosphere to obtain Cu/CoO$_x$ @NFs. The samples were named as Cu/CoO$_x$ @NFs-20, Cu/CoO$_x$ @NFs-40 and Cu/CoO$_x$ @NFs-60 according to the reduction and reconstitution time.

2.2.2.2. Preparation of comparative catalysts Cu-CoO$_x$ @NFs and Cu/CoO$_x$. To verify the interaction between CuCo-PBAs and PAN, two comparative samples were prepared, labeled as Cu-CoO$_x$ @NFs and Cu/CoO$_x$, respectively. Specifically, while keeping the mole fraction of cobalt/copper cations in the precursor solution unchanged, a certain amount of copper chloride and cobalt chloride are added to the DMF solvent instead of CuCo-PBAs. The remaining steps are the same as above, sample denoted as Cu-CoO$_x$ @NFs. Using CuCo-PBAs as the precursor without electrospinning and the above steps are repeated, denoted as the control sample Cu/CoO$_x$.

2.2.2.3. Preparation of comparative catalyst CoO$_x$ @NFs. To verify the active element of the electrocatalyst, CoCo-PBAs was used instead of CuCo-PBAs as the precursor of the spinning solution, and the preparation steps above were repeated to obtain the comparison sample CoO$_x$ @NFs.

2.2.2.4. Preparation of comparative catalysts Cu$_{0.5}$/CoO$_x$ @NFs and Cu/Co$_{0.5}$O$_x$ @NFs. In order to obtain the best electrocatalytic performance, the proportion of copper and cobalt in the electrocatalyst was regulated. The specific operation is to change the spinning precursors, using Cu$_{0.5}$Co$_1$-PBAs and Cu$_1$Co$_{0.5}$-PBAs as the spinning liquid precursors, and the other steps are the same as above, and the products are written as Cu$_{0.5}$/CoO$_x$ @NFs and Cu/Co$_{0.5}$O$_x$ @NFs, respectively.

2.3. Materials characterization

XRD were obtained using a Bruker D8 Discover X-ray diffractometer with Cu Kα radiation (λ = 1.5418 Å). X-ray photoelectron spectroscopy (ESCALAB250) was used to analyze the valency-state of elements. The chemical states of the different elements were determined by using a Thermo VG ESCALAB 250 X-ray photoelectron spectrometer equipped with Al-Ka X-ray radiation. The morphology and microstructure of the

electrocatalysts were observed by field emission scan electronic microscopy (JEOL JSM-7800 F) and high-resolution transmission electron microscope (JEOL JEM-F200). The BET surface area and pore size distribution were determined by using a Gas and vapor adsorption apparatus (BEL SORP-max). Electron paramagnetic resonance (EPR) spectra were collected on a Bruker emxplus. Ultraviolet photoelectron spectroscopy (UPS) measurements were conducted using a Thermo Fisher Nexsa with a He (I) photo line of 21.22 eV. Ultraviolet–visible (UV–vis) spectroscopy measurements were performed using a Perkin Elmer Lambda 750 on diffuse reflectance mode and a Shimadzu UV-2550. The surface potential was investigated by Kelvin Probe Force Microscopy (Bruker MultiMode8) and Zeta potential were investigated by Malvern Zetasizer (ZEN3600). Gas by-products were measured by gas chromatograph (GC-9890b). Nuclear magnetic resonance (NMR) spectroscopy was performed on a Bruker 500 MHz NMR spectrometer (Ascend 400).

2.4. Electrochemical measurements

A typical three-electrode system was set up in the H-type electrolytic cell for the electrocatalytic nitrate reduction tests, and all the electrochemical tests were performed on an electrochemical workstation (CHI 760E). Specifical, Pt foil and Hg/HgO are used as counter and reference electrodes, respective, and both of them were placed in the anodic chamber. The clean carbon paper coated with catalysts (mass loading: 1 mg cm^{-2}) was used as working electrode and placed in the cathodic chamber. The trimmed FAB-PK-130 anion exchange membrane was used as a separator between cathode and anode. In order to avoid the influence of air on the reduction process, Ar gas was continuously pumped into the electrolyte during the test. According to Nernst equation, all the electric potentials in the experiment were approximately converted according to the following equation:

$$E_{(RHE)} = E_{(Hg/HgO)} + 0.098 + 0.059 \times pH$$

Unless otherwise stated, all electrocatalytic materials in this paper have been activated by cyclic voltammetry (CV) before testing, and the linear sweep voltammetry curves have been tested at a scan rate of 5 mV s^{-1}. All LSV curves have been corrected by iR correction. The electrochemical active surface area (ECSA) of the electrocatalysts were evaluated by CV in the non-Faradaic current region by varying the scanning rate. Electrochemical impedance spectroscopy (EIS) measurements were performed at a constant potential of -0.075 V_{RHE} and in the frequency range from 1 MHz to 1 Hz.

2.5. Ammonia/nitrate detection and faradaic efficiency calculations

The quantification of ammonia in the product electrolyte diluted at a certain multiple was performed by the indophenol blue method as reported in the relevant literature [36]. (Among them, the product electrolyte of all catalysts was diluted 5 times, except for the product electrolyte of CoO$_x$@NFs catalyst which was diluted 3 times). This method uses a mixture of 0.36 M salicylic acid, 0.36 M NaOH and 0.18 M potassium sodium tartrate as the coloring agent. At room temperature, 8 ml of the diluted product electrolyte was taken and 1 ml of colorant, 100 μL of aqueous sodium nitroprusside (0.034 M), 100 μL of NaClO solution (6–14% effective chlorine content) and 100 μL of NaOH solution (0.75 M) were added to it sequentially. After standing the above solution away from light for 1 h to ensure complete coloring, the absorbance of the solution was determined by ultraviolet spectrophotometer. The maximum absorption wavelength of ammonia appeared at about 670 nm. Before coloring the product electrolyte, a series of ammonia standard solutions of known concentration were prepared and their absorbance was measured to obtain a linear relationship between known ammonia concentration and absorbance, i.e., a standard curve (Fig. S6a). The ammonia content in the product electrolyte can be

derived from this standard curve. For the qualitative detection of NO$_2^-$ and the advanced product N$_2$H$_4$ in the liquid product the classical Griess method [37] and the Watt & Chrisp method [38] reported in the literature were used, respectively.

The concentrations of NO$_3^-$ were detected by UV−vis spectrophotometer. The nitrate removal percentage (R) was calculated by the equation:

$$R = (C_0\text{-}C_t/C_0) \times 100\%$$

where C_0 (mg/L) and C_t (mg/L) are the initial nitrate concentration and its concentration at time t, respectively.

Ammonia Faradaic efficiency was calculated according to the following equation:

$$\text{Faradaic efficiency} = nV_{catholyte}C_{NH3}F/Q$$

where n is the number of transferred electrons for the generation of 1 mol of ammonia which is 8; $V_{catholyte}$ stands for the volume of liquid product (ml), and the value is 25 ml; C_{NH3} represents the concentration of ammonia (M); F is the Faraday constant (96485 C mol^{-1}); Q represents the total consumed charge (Q = it).

2.6. Computational methods and details

All the computations were performed by using Vienna ab initio simulation package (VASP) [39,40]. The ion-electron interactions were described by the projector augmented wave method [41] and the general gradient approximation in the Perdew-Burke-Ernzerhof (PBE) form was used [42,43]. The wavefunctions were expanded in a plane wave basis with an energy cutoff of 400 eV, using the projector augmented wave (PAW) method. During the structure relaxation, the convergence criterion was set to 0.03 eV/Å and 10^{-5} eV for the residual force and energy, respectively. A 3-layered Cu (111) slab deposited on a $2 \times 2 \times 1$ Co$_3$O$_4$ (111) slab was used as the model for Cu/Co$_3$O$_4$ (pristine). On this basis, 3, 6 and 9 of 16 O atoms on the interface of Cu (111) and Co$_3$O$_4$ (111) were removed to simulate O vacancy-rich Cu/Co$_3$O$_4$ (labelled as Cu/Co$_3$O$_4$ (3 O$_v$), Cu/Co$_3$O$_4$ (6 O$_v$) and Cu/Co$_3$O$_4$ (9 O$_v$)). Brillouin zones were sampled by $3 \times 3 \times 1$ and $5 \times 5 \times 1$ Monkhorst-Pack k-point grid for the structure optimization and electronic structure computations. To avoid the interaction between two periodic units, a vacuum space over 15 Å was employed.

The adsorption energy of H2O (ΔE_{H2O}) was calculated as:

$$\Delta E_{H2O} = E_{*H2O} - E_* - E_{H2O}$$

where E_{*H2O} and E_* are the total energy of material with and without H2O adsorption, respectively, and E_{H2O} is the energy of H2O molecule.

The free energy for hydrogen adsorption (ΔG_H) was calculated as:

$$\Delta G_H = \Delta E + \Delta E_{ZPE} - T\Delta S$$

where ΔE, E_{ZPE}, T and S is the hydrogen adsorption energy, zero-point energies, temperature and entropy, respectively.

For the dissociation of H2O, H2O and OH + H adsorbed structures were used as the initial state (IS) and final state (FS), respectively. The climbing nudged elastic band method [44,45] was used to search the structure of transition state (TS). The energy barrier for H2O dissociation (Ea) was the energy difference between the TS and IS:

$$Ea = ETS - EIS$$

The adsorption energies were calculated by using the following equation：.

$$E_{ads} = E_{total} - E_{sub} - E_{mol}$$

where E_{total} is the total energy of substrates and NO$_3$ adsorbate and E_{sub} is the energy of substrates and E_{mol} is the energy of NO$_3$ molecular.

The Φ was defined as the difference between the vacuum level

(E_{vacuum}) and Fermi level (E_{Fermi}): $\Phi = E_{vacuum} - E_{Fermi}$.

3. Result and discussion

3.1. Theoretical calculation investigation

Recent studies have indicated that electrocatalysts based on metallic copper are highly selective for the reduction of nitrate ions (NO_3^-) to produce ammonia (NH_3) in NO_3^-RR [46,47]. However, the weak water-dissociation ability of Cu greatly limits its proton transfer and reaction kinetics in the NO_3^-RR [48,49]. It is well known that metal oxides (i.e., Co_3O_4) are highly active for water dissociation [50,51]. Therefore, we hypothesized that the creation of Cu/Co_3O_4 hetero-interfaces might simultaneously tune the electronic structure of Cu and promote proton transfer, thereby substantially enhancing the NO_3^-RR activity. Subsequently, we used DFT calculations to investigate the factors that induce changes in $\Delta\Phi$ between heterogeneous interfacial structures and changes in the local electron structure. The effect of O_v on the synergistic effect of $\Delta\Phi$ and the heterostructure was investigated. First, Cu (111) and Co_3O_4(111) (without and with different O_v concentrations) were combined to create heterogeneous interfacial structural models. The optimized structural models are shown in Fig. 1(a)–(d) and Fig. S1. The four models are denoted as Cu/Co_3O_4 (pristine), Cu/Co_3O_4 (3 O_v), Cu/Co_3O_4 (6 O_v), and Cu/Co_3O_4 (9 O_v) based on their O_v concentrations. It was discovered that when the optimized structural model had a high O_v concentration (i.e., 9 O_v), the Cu (111) structural model changed substantially to the extent that the overall heterogeneous interfacial structure appeared to be highly irrational. In other words, the O_v concentration in heterogeneous interfacial structures has a limit that cannot be increased indefinitely. The overall structure and properties exhibited were the most stable when a certain degree of equilibrium is reached [52]. Subsequently, the $\Delta\Phi$ of the several Cu/CoO_x heterogeneous interface model was studied using calculations. The $\Delta\Phi$ results for each model were shown in Fig. 1(e) and Fig. S2. Cu/Co_3O_4 (3 O_v), Cu/Co_3O_4 (6 O_v), and Cu/Co_3O_4 (9 O_v) had $\Delta\Phi$ values of 1.89, 1.33, and 1.69, respectively. The fact that Cu/Co_3O_4 (6 O_v) exhibited the smallest $\Delta\Phi$ value may be a key factor in providing strong

theoretical support for its excellent electrocatalytic reduction performance. Meanwhile, the Bader charge analysis further confirmed the change in the local electronic structure at the Cu/CoO_x heterogeneous interfaces. The results (Fig. 1(f)) demonstrated that Co_3O_4 acted as a charge collector for the Cu/Co_3O_4 and Cu/Co_3O_4 (O_v) heterogeneous interfacial structures through the electronic interactions between the localized Cu–O–Co bonds, attracting electrons from the Cu nanoparticles and transferring them to Co_3O_4. As the O_v concentration increased, the number of electrons that were transferred from Cu to Co_3O_4 gradually decreased, and the total charge of Cu gradually increased from Cu/Co_3O_4 (pristine) to Cu/Co_3O_4 (3 O_v) and Cu/Co_3O_4 (6 O_v), showing a trend of electron enrichment.

Previous studies have shown that changes in the *d*-band center affect the adsorption and modulation of *H on the surface of heterogeneous structures [53,54]. Fig. 1(g) shows the PDOS diagram of the *d* orbitals of the Cu atoms in the four structural models calculated using DFT. The calculated values of the *d*-band centers were − 2.11 (Cu/Co₃O₄ (pristine)), − 2.15 (Cu/Co₃O₄ (3 O_v)), − 2.19 (Cu/Co₃O₄ (6 O_v)), and − 2.24 eV (Cu/Co₃O₄ (9 O_v)), respectively, all of which span the Fermi energy level. These values confirmed the formation of O_v in the Cu/CoO_x heterogeneous interfacial structure and the change in the local electronic structure. Additionally, the DFT calculations revealed that the introduction of O_v also affects the electronic structure of CoO_x. Compared to Cu/Co_3O_4 (pristine), the other models caused the *d*-band center of Co to move near the Fermi energy level and optimized the adsorption energy of Co_3O_4 (O_v) toward key intermediates (*OOH) of water decomposition, which could better promote its adsorption and dissociation of water molecules. The calculated results demonstrated that the Cu atoms in the Cu/Co_3O_4 (6 O_v) structural model had moderate *d*-band center values, indicating that the reactants and reactive intermediates underwent a mild adsorption/desorption process [36]. The *d*-band center theory [53], revealed that the ideal binding energy was neither strong nor weak, and the binding energy between the adsorbate and adsorbent was found to be closely related to the highly localized metal electronic states. In comparison, the Co atom in the Cu/Co_3O_4 (6 O_v) structural model had a *d*-band center value that was closer to the Fermi energy level. It was confirmed that the dissociation of water
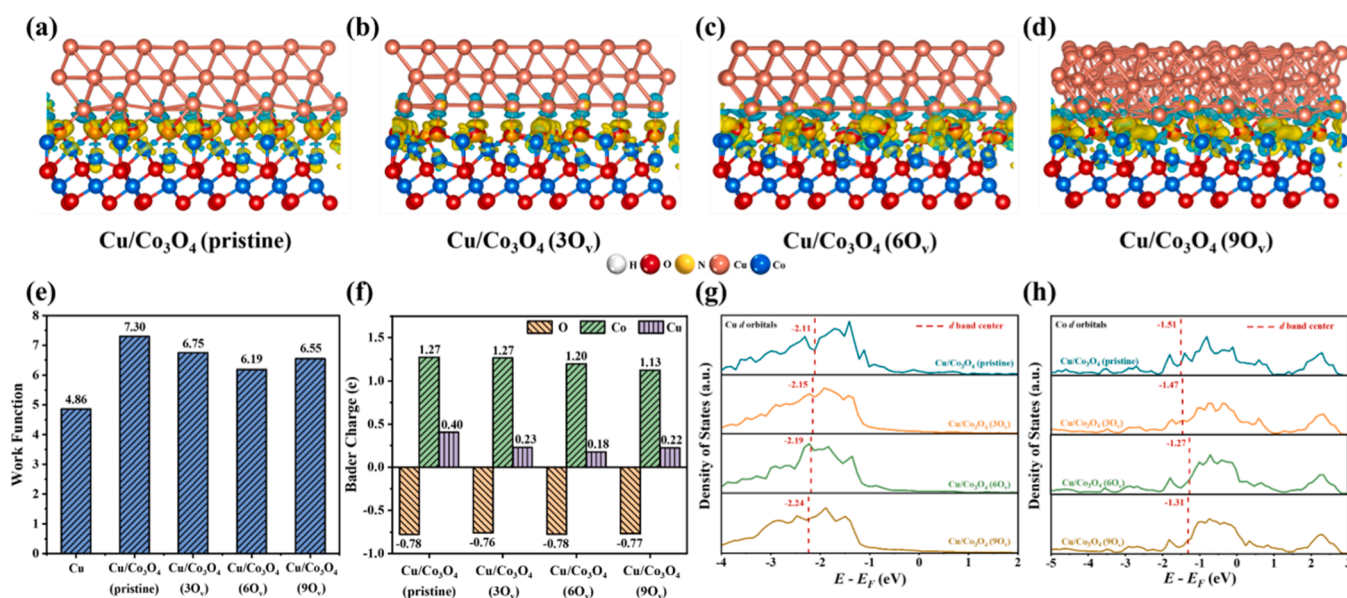

Fig. 1. Isosurfaces of charge-density difference of (a) Cu/Co₃O₄ (pristine), (b) Cu/Co₃O₄ (3 O_v), (c) Cu/Co₃O₄ (6 O_v), and (d) Cu/Co₃O₄ (9 O_v). The isosurface value is set to 0.005 e/Bohr³, and the charge accumulation and depletion are shown in yellow and cyan, respectively. (e) Work function results for Cu, Cu/Co₃O₄ (pristine), Co₃O₄ (3 O_v), Co₃O₄ (6 O_v), and Co₃O₄ (9 O_v) obtained through calculations. (f) Computed Bader charges (average values) of the Co, O, and Cu atoms in Cu/Co₃O₄ (pristine), Cu/Co₃O₄ (3 O_v), Cu/Co₃O₄ (6 O_v), and Cu/Co₃O₄ (9 O_v). The positive and negative values indicate charge loss and gain, respectively. (g, h) Calculated projected density of states (PDOS) of the *d* orbitals of the interfacial Cu and Co atoms in Cu/Co₃O₄ (pristine), Cu/Co₃O₄ (3 O_v), Cu/Co₃O₄ (6 O_v), and Cu/Co₃O₄ (9 O_v). The Fermi levels are set to 0 eV, and the red dashed lines represent the calculated *d*-band center.

molecules and the formation of *H could be effectively induced when the O_v concentration in Co_3O_4 reached a stable state (Fig. 1(h)). Altogether, the aforementioned results confirmed the strong correlation between the O_v-induced changes in the local electronic structure of Cu and Co_3O_4 and the positive effect of moderate O_v concentrations on the $\Delta\Phi$ and electron transfer in the heterogeneous interfacial structure.

3.2. Structural and morphology characterization

To test the above theoretical concept, we designed a one-dimensional multiporous nanofiber (Cu/CoO_x @NFs) electrocatalyst model with a Cu/CoO_x-rich heterogeneous interface. The synthesis schematic is shown in Fig. 2(a). Binary copper–cobalt Prussian blue analogs (CuCo-PBAs) were used as precursors and shaped into nanofiber structures using an electrostatic spinning technique. The CuCo-PBA-coated nanofibers were pre-oxidized at 280 ℃ and then subjected to high-temperature heat treatment at 500 ℃ for 2 h. Thereafter, they underwent size reduction and PAN removal to produce one-dimensional interconnected multi-porous nanofibers that were rich in the CuO/Co_3O_4 heterogeneous interfacial structure. The CuO/Co_3O_4 heterogeneous interface was finally reconstructed into a Cu/CoO_x (with O_v) heterogeneous interface in a reducing atmosphere. The reduction and reconstruction times were controlled to adjust the O_v concentration in the Cu/CoO_x heterogeneous interfacial structure in order to affect the $\Delta\Phi$. SEM and TEM characterizations were performed to analyze the morphological and structural properties of the Cu/CoO_x @NFs. The results were shown in Figs. 2(b), 2(c), and 2(e). It could be observed that the Cu/CoO_x @NFs comprised interconnected Cu/CoO_x hetero-structured nanoparticles with a diameter of about 50 nm, forming 500 nm nanofibers with a regular distribution and abundant pore channels. Subsequently, the active catalyst was characterized using visual HRTEM and TEM mapping (Figs. 2(d), 2(f), and 2(g)). The measured lattice fringe spacing in the HRTEM image showed that the Cu/CoO_x heterogeneous structure nanoparticles that were distributed on the fiber of the interconnected multi-pores mainly existed as Cu (111) and Co_3O_4 (111) crystal planes and formed a clear heterogeneous interfacial structure. This was also confirmed by the XRD results for the Cu/CoO_x @NFs (Fig. S3(c)). The TEM mapping results revealed that the

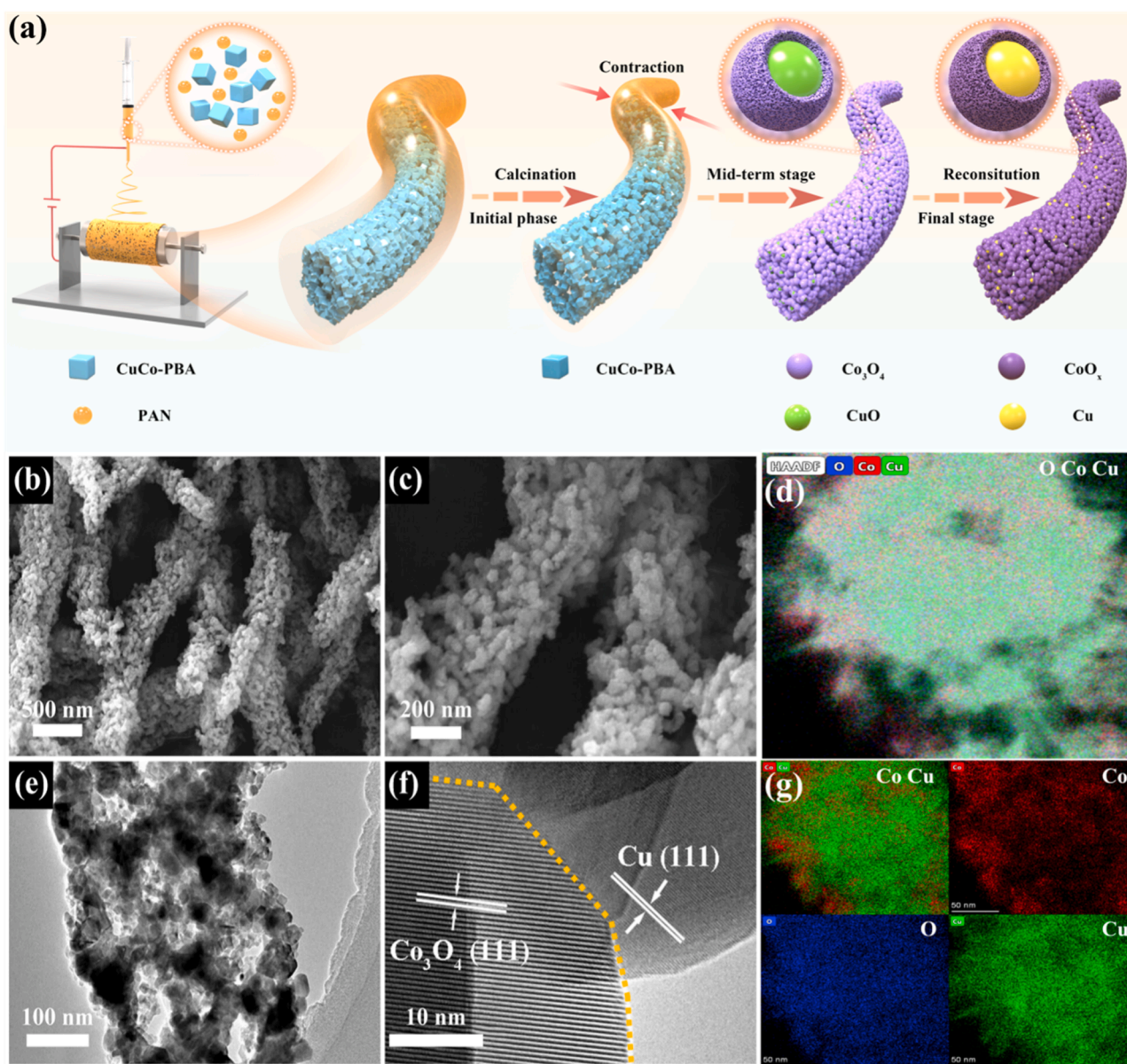**Fig. 2.** (a) Schematic of the synthesis process for the rich Cu/CoO_x @NFs heterogeneous active electrocatalyst. (b, c) SEM, (e, f) HRTEM, and (d, g) elemental distribution mapping images of the Cu/CoO_x @NFs.

Cu, Co, and O elements were uniformly distributed in the Cu/CoO$_x$ @NFs structure. In particular, the Co distribution differed from the Cu distribution, and the two elements formed a very noticeable interface boundary. It was further confirmed that the active electrocatalyst was a heterogeneous interface-rich structured nanofiber comprising Cu as an elemental substance and Co$_3$O$_4$ as an oxide, which corroborates with the HRTEM results (Fig. 2(f)).

The phase and structure of the CuCo-PBAs and other comparison precursors were analyzed using XRD analysis (Figs. S3(a), S4(a), and S4 (b)). By calculating the corresponding lattice parameters, it was discovered that all the PBAs were face-centered cubic crystal structures. The XRD results also corresponded to Cu$_3$[Co(CN)$_6$]$_2$ (JCPDS no. 5–1895), and Co$_3$[Co(CN)$_6$]$_2$ (JCPDS no. 22–0215), which were similar to the Prussian blue crystal structures that have been reported in the literature [35,55]. The XRD patterns (Figs. S3(b), S4(c), and S4(d)) revealed that CuCo-PBA@PAN with the corresponding reference samples were all converted into nanofibers rich in Co$_3$O$_4$ (JCPDS no. 80–1532) and CuO (JCPDS no. 48–1548) heterogeneous interfacial structures after the high-temperature treatment process. Subsequently, the remodeling effect of the reducing atmosphere caused the heterogeneous interfacial structure to gradually transform from CuO/Co$_3$O$_4$ to Cu/CoO$_x$ (Cu (JCPDS no. 85–1326) and Co$_3$O$_4$ (JCPDS no. 80–1532)), and this change was also confirmed by the XRD results (Fig. S3(c)). The reconstruction time greatly affected the O$_v$ concentration and the electronic structure inside the Cu/CoO$_x$ heterogeneous interface. The XPS results (Figs. S3(d) and S3(f)) showed that after the gradient reconstruction time was adjusted, the $2p_{3/2}$ and $2p_{1/2}$ peaks of Cu in the Cu/CoO$_x$ heterogeneous interface gradually shifted toward the low-binding-energy region, while the $2p_{3/2}$ and $2p_{1/2}$ peaks of Co gradually shifted toward the high-binding-energy region, confirming that the reconstruction effect induced changes in the electronic structure inside the Cu/CoO$_x$ heterogeneous interface. Moreover, the peak area corresponding to the O$_v$ concentration shown in Fig. S3(e) increased gradually, further confirming the positive relationship between the reconstruction time and the O$_v$ concentration.

To investigated the influence of the precursors on the morphology and structural construction of the electrocatalysts (Fig. S5), comparison samples, Cu-CoO$_x$ @NFs, were synthesized using the same molar fraction of Cu/Co salts. These samples were characterized accordingly. Fig. S6 showed the SEM images of the Cu-CoO$_x$ @NFs. It could be observed that the Cu-CoO$_x$ @NFs had a diameter of about 1.2 μm, which was about twice that in Cu/CoO$_x$ @NFs. Due to the presence of densely packed larger nanoparticles, the porosity of Cu-CoO$_x$ @NFs is relatively low. This may be because CuCo@PAN was electrostatically reduced owing to the instability of bivalent copper during electrospinning at a high voltage, and an agglomeration phenomenon occurred between the mixed metal-oxide particles during the calcination process. The above-mentioned analysis results demonstrated that the Cu/CoO$_x$ @NFs possessed interconnected and porous nanofiber structures because of the special pyrolysis effect of the CuCo-PBAs during air calcination. Additionally, precursors containing only Co metal (CoCo-PBAs) and comparison samples (CoO$_x$ @NFs) were prepared to confirmed if Cu was the main active site for the NO$_3^-$RR (Figs. S5(a), S5(b), and S7). The CoCo-PBAs exhibited similar pyrolysis behavior to the CuCo-PBAs, which caused the nanofibers obtained after roasting to also exhibited porous interconnectivity. The XRD test results (Fig. S4(c)) showed that the CoO$_x$ @NFs were nanofiber structures containing Co$_3$O$_4$ (JCPDS no. 74–2120) as the main component. The Cu/Co ratio of the CuCo-PBA precursors was regulated to obtain the best reductive catalytic performance from the active electrocatalysts. The corresponding precursors (Cu$_1$Co$_{0.5}$-PBAs and Cu$_{0.5}$Co$_1$-PBAs) (Fig. S5(b)–S5(d)) and comparison samples (Cu$_{0.5}$/CoO$_x$ @NFs and Cu/Co$_{0.5}$O$_x$ @NFs) were synthesized. The adjustment of the Cu/Co ratio caused a dramatic change in the size of the corresponding PBAs, which resulted in a large difference in the size of the associated nanofibers (Fig. S8). The XRD results revealed that the two comparison samples were broadly similar to the Cu/CoO$_x$ @NFs in

terms of physical phase. It was hypothesized that the difference in the morphological structure and the ratio of active ingredients may had a substantial effect on their electrocatalytic reduction performance.

3.3. Electrocatalytic performance investigation for NO$_3^-$RR

All the above mentioned prepared electrocatalysts were further tested for electrocatalytic NO$_3^-$ reduction. Specifically, the NO$_3^-$RR tests were performed in electrolytes with and without NO$_3^-$ to determine the actual catalytic activity of the samples. First, the relevant LSVs of the Cu/CoO$_x$ @NFs and Cu-CoO$_x$ @NFs were determined. The LSV curves (Figs. 3(a), 3(b) and Fig. S9(a)–S9(c)) confirmed that the two electrocatalysts exhibited the corresponding NO$_3^-$RR activity in the electrolyte containing NO$_3^-$, indicating that the current density of the electrocatalysts mainly originated from the NO$_3^-$RR rather than the HER. The Cu/CoO$_x$ @NFs had a substantially higher current density than the other comparison samples, indicating that they exhibited higher NO$_3^-$RR catalytic activity. Secondly, corresponding LSV tests were conducted on the CoO$_x$ @NFs samples without Cu (Fig. S9(d)). Evidently, the absence of Cu significantly impeded the performance of the electrocatalyst, thus confirming that Cu is the primary active site responsible for the NO$_3^-$RR taking place in the active electrocatalyst. To determine the sample with the best NO$_3^-$RR performance, LSV tests were also conducted on the Cu$_{0.5}$/CoO$_x$ @NFs and Cu/Co$_{0.5}$O$_x$ @NFs samples with different Cu/Co ratios (Figs. S9(e) and S9(f)). Although the NO$_3^-$RR catalytic activity of the Cu/Co$_{0.5}$O$_x$ @NFs was superior to that of the Cu$_{0.5}$/CoO$_x$ @NFs, it was still considerably lower than the optimal activity of the Cu/CoO$_x$ @NFs sample. The relatively poor performance of these two samples may have been due to the synergistic effect of the different Cu/Co ratios and the different morphologies and structures of the different nanofibers. Additionally, the effects of different O$_v$ concentrations on the performance of the active electrocatalysts were compared (Fig. 3(c)). The results revealed that the gradient O$_v$ concentration is proportional to the electrocatalytic reduction performance, further confirming that the O$_v$ concentration in the stable state of the sample has a substantial promotion effect on the NO$_3^-$RR performance.

Generally, electrocatalytic reduction reactions often occur in gas-liquid-solid multiphase interfaces [56]. Nanofiber structures with many pores and large specific surface areas can effectively increase the charge-transfer capacity and promote the mass-transfer process [57]. Based on this, the active electrocatalysts and their comparison samples were tested for their bilayer capacitance (Figs. S10 and S11), and the Cu/CoO$_x$ @NFs sample displayed the best performance. Interconnected porous nanofiber structures are known to effectively promote the NO$_3^-$-to-NH$_3$ mass transfer process and charge transfer, which could fully expose the active site of the electrocatalyst and effectively increase its intrinsic activity. Therefore, electrochemical impedance spectroscopy (EIS) tests were performed on all Cu/CoO$_x$ @NFs samples at a reduction potential of $j = 100$ mA cm^{-2} (i.e., -0.10 V$_{RHE}$) to evaluate the effect of their electrochemical charge-transfer resistance on their catalytic performance (Fig. 3(i)). The Cu/CoO$_x$ @NFs supported the dual effect of interconnected multiporous nanofiber structures and Cu/CoO$_x$ active heterogeneous interfacial structure with minimal resistance results, which effectively reduced the charge-transfer resistance exhibited during the NO$_3^-$RR. Additionally, low-temperature N$_2$ adsorption–desorption tests were conducted to investigate the specific surface area and pore-size distribution of the corresponding nanofiber structure samples. As shown in Fig. S12 and S13, the participating test samples were all nanofiber structures containing mesopores or even macropores, and the optimal active electrocatalyst, Cu/CoO$_x$ @NFs, also had a substantially higher specific surface area than the other comparison samples.

Another criterion for measuring the performance of an active electrocatalyst for the NO$_3^-$RR is the FE of its product (NH$_3$) [58]. The abovementioned electrocatalysts were quantified for the ideal NH$_3$ product using existing methods. The electrocatalysts were electrolyzed
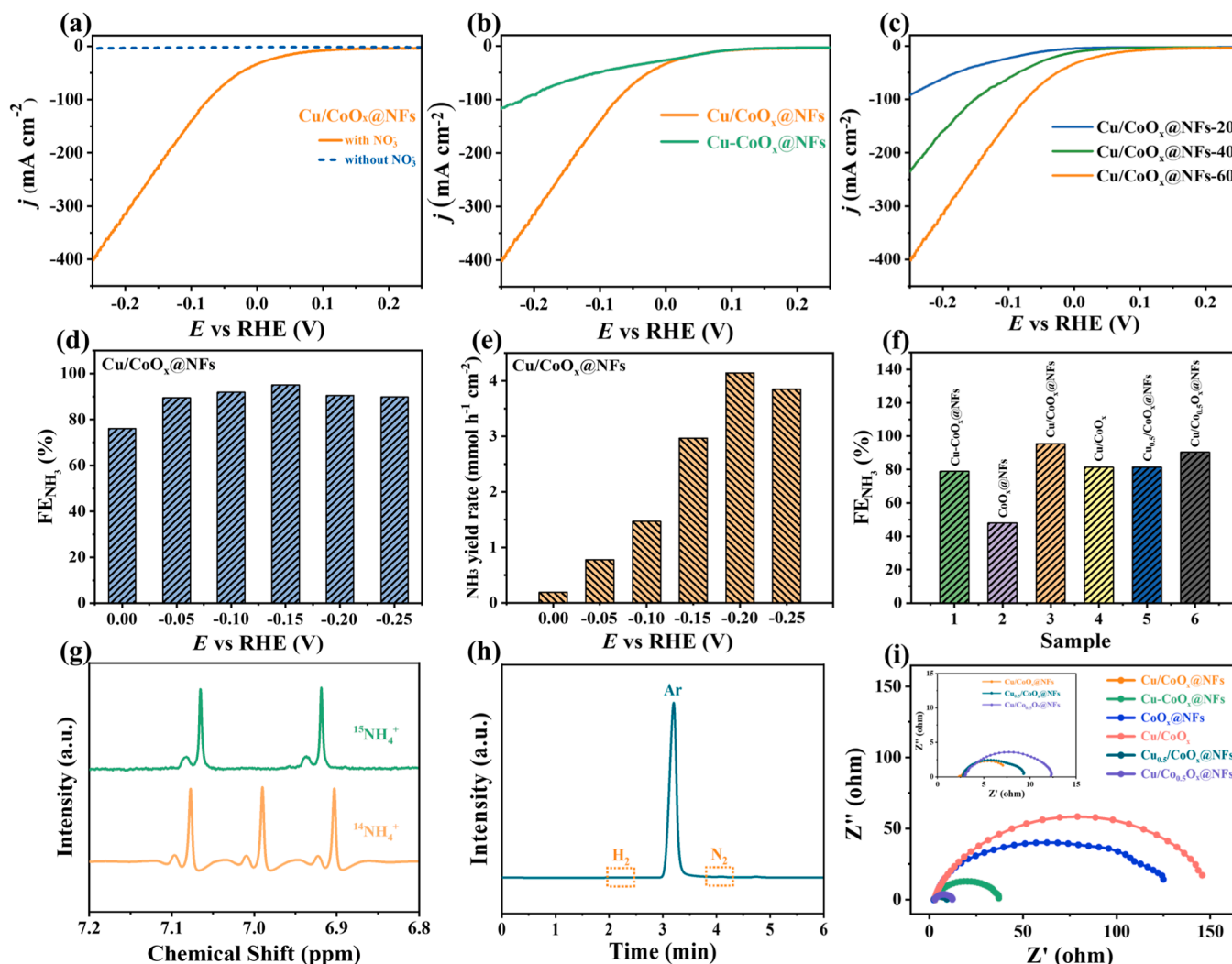
Fig. 3. (a) LSV of the Cu/CoO$_x$ @NFs in 1 M KOH with and without 0.1 M NO$_3^-$. (b) LSV comparison of the Cu/CoO$_x$ @NFs and Cu-CoO$_x$ @NFs in 1 M KOH with 0.1 M NO$_3^-$. (c) LSV comparison of Cu/CoO$_x$ @NFs-20, Cu/CoO$_x$ @NFs-40, and Cu/CoO$_x$ @NFs-60 in 1 M KOH with 0.1 M NO$_3^-$. (d) FE$_{NH3}$ and (e) NH$_3$ yield rate of the Cu/CoO$_x$ @NFs for the NO$_3^-$RR in 1 M KOH with 0.1 M NO$_3^-$. (f) FE$_{NH3}$ of the Cu/CoO$_x$ @NFs and their comparison samples for the NO$_3^-$RR in 1 M KOH with 0.1 M NO$_3^-$. (g) 1 H NMR spectra of liquid products obtained through the NO$_3^-$RR of ^{14}N NO$_3^-$ and ^{15}N NO$_3^-$ as reactants. (h) Representative gas chromatograph of gas products obtained on the Cu/CoO$_x$ @NFs. (i) EIS Nyquist plots of the Cu/CoO$_x$ @NFs electrocatalysts and their comparison samples for the NO$_3^-$RR at the reaction potential of 100 mA cm^{-2} (−0.075 V$_{RHE}$).

for 1 h at the potential range of − 0.25–0 V$_{RHE}$ at intervals of 0.05 V$_{RHE}$ (Fig. S14). Finally, ultraviolet–visible (UV–Vis) spectroscopy was used to quantitatively analyze NH$_3$ in the electrolyte of the cathode products. The Cu/CoO$_x$ @NFs and other comparison samples were electrolyzed at various potentials of 0, − 0.05, − 0.10, − 0.15, − 0.20, and − 0.25 V$_{RHE}$ for 1 h, respectively, and then the collected electrolyte was diluted to a certain multiple. After complete colorant staining, the absorbance was measured using ultraviolet spectrophotometry. The dyed electrolyte underwent different degrees of color change, and the larger the NO$_3^-$ concentration the darker the electrolyte color. The NH$_4^+$ content in the electrolyte product was quantitatively analyzed by comparing it with the standard curve (Fig. S15). The FE and NH$_3$ production rates of the product were further calculated (Figs. 3(d)–3(f) and S16–S17). The results showed that the FE of all the aforementioned electrocatalysts exhibited an increasing trend in the low-voltage range, while the FE and NH$_3$ production rate of the electrocatalysts exhibited a peak plateau or even a decreasing trend when the working potential reached − 0.20 V$_{RHE}$ (Figs. S16 and S17). It is noteworthy that the FE of the Cu/CoO$_x$ @NFs reached its maximum value at the reaction potential of − 0.15 V$_{RHE}$, demonstrating that the Cu/CoO$_x$ @NFs exhibited superior

performance to the vast majority of transition metal-based electrocatalytic materials reported in the literature on the NO$_3^-$RR [59–64].

In addition to using UV–Vis spectroscopy to quantitatively and qualitatively analyze the NH$_3$ product, nuclear magnetic resonance spectroscopy (NMR) was also used to qualitatively determine the NH$_3$ product using isotope tracer technology to further improve the accuracy of the experiment. For this purpose, 1 M KOH containing 0.1 M ^{15}NO$_3^-$ or 0.1 M ^{14}NO$_3^-$ was used as the electrolyte, and overnight operations were performed continuously at a potential of − 0.15 V$_{RHE}$ to collect the electrolyte product and conducted isotopic tracing. The ^{1}H NMR spectra (Fig. 3(g)) revealed that three peaks appeared in the electrolyte curve of the product containing ^{14}NO$_3^-$, while the electrolyte curve of the product containing ^{15}NO$_3^-$ split into two peaks. This was consistent with a previous finding [65,66] and provided strong evidence that NH$_3$ originates from the NO$_3^-$RR. According to an existing literature report [67], the electrocatalytic NO$_3^-$-to-NH$_3$ reaction process may be accompanied by the production of NO$_2^-$, N$_2$, hydrazine (N$_2$H$_4$), and other by-products, as well as the influence of the competitive HER. In this study, we only qualitatively analyzed the products of the optimal active electrocatalyst, Cu/CoO$_x$ @NFs. The production of NO$_2^-$ as a by-product in the liquid

product was examined using the classical Griess method reported in the literature [37]. The UV–Vis spectrum (Fig. S18) of the electrolyte product showed no appearance of any characteristic peak in the spectral range of 450–660 nm, confirming that there was no NO_2^- by-product in the liquid product. Generally, N_2H_4 is the advanced liquid-phase product of the NO_3^--to-NH_3 reaction. The electrolyte product was qualitatively analyzed using the classical Watt and Chrisp method [38], to detect the presence of N_2H_4. The corresponding UV–Vis spectrum did not reveal any characteristic peaks in the corresponding range, confirming the absence of advanced N_2H_4 product formation in the product (Fig. S18). To verify if gas-phase by-products were formed during the electrochemical reduction process, the cathode chamber gas was analyzed using gas chromatography (GC) with Ar as the carrier gas. The GC patterns (Fig. 3(h)) displayed only the peak of the Ar carrier gas and no characteristic peaks of the N_2 by-product or the competing H_2 reaction products, indicating that no gas-phase by-products were generated in the products of the Cu/CoO_x @NFs electrocatalyst. The above-mentioned results fully confirmed that the active electrocatalyst, Cu/CoO_x @NFs, possesses extremely high product selectivity. In addition, we have tested the NO_3^- removal rate during the NO_3^-RR on Cu/CoO_x @NFs. The result indicated that Cu/CoO_x @NFs has good ability to transform NO_3^- to NH_3, and nearly all the NO_3^- could be converted to NH_3 within 12-h continuous electrolysis. (Fig. S19).

3.4. Mechanism investigation for NO_3^-RR

The reconstructed sample underwent individual characterization using electron paramagnetic resonance (EPR) to visually confirm the presence of O_v in the Cu/CoO_x @NFs. The samples obtained after different degrees of reductive reconstruction were labeled as Cu/CoO_x @NFs-20, Cu/CoO_x @NFs-40, and Cu/CoO_x @NFs-60. The results showed that the three samples exhibited a gradient in O_v concentration

after reductive reconstruction (Fig. 4(d)), which was consistent with the XPS results. The Cu/CoO_x @NFs-60 sample had a higher O_v concentration than the $CuCoO_x$ @NFs-20 and Cu/CoO_x @NFs-40 samples. During the reductive reconstruction process, in addition to the gradual reduction of CuO to Cu, the O_v concentration in Co_3O_4 also gradually increased until a steady state was attained, and then interconnected multiporous nanofibers rich in the Cu/CoO_x heterogeneous interfacial structure were formed.

To verify the effect of different O_v concentrations on the $\Delta\Phi$ between the heterogeneous interfacial structures, Co_3O_4 containing different O_v concentrations was prepared using the same reductive reconstruction strategy. The resulting samples were labeled as CoO_x-20, CoO_x-40, and CoO_x-60 and characterized by ultraviolet photoelectron spectroscopy (UPS) (Fig. S20). The results revealed that the work functions of Cu, CoO_x-20, CoO_x-40, and CoO_x-60 were 4.03, 4.15, 4.11, and 4.04, respectively, and the corresponding $\Delta\Phi$ values were 0.12, 0.08, and 0.01 (Fig. 4(c)). Previous results have shown that $\Delta\Phi$ could provide a moderate thermodynamic and kinetic barrier within a certain range, and a small $\Delta\Phi$ between heterostructures could attenuate electron accumulation at the interface, thus promoting *H transfer and enhancing synergistic effects [30]. Therefore, we demonstrated that the introduction of O_v can change the $\Delta\Phi$ values between the heterogeneous interfacial structures, thereby affecting the transfer of electrons and *H and promoting the electrocatalytic reduction process. The abovementioned results corresponded to the DFT calculation results. Owing to the limitations in the selection of the crystal plane during the calculation process, the calculated work function values of CoO_x containing different O_v concentrations were generally large, resulting in a large difference between the calculated $\Delta\Phi$ values and the experimental $\Delta\Phi$ values, but their overall change trends exhibited the same performance and maintained a strong correspondence.

We further investigated the effect of $\Delta\Phi$ on *H transfer on the surface

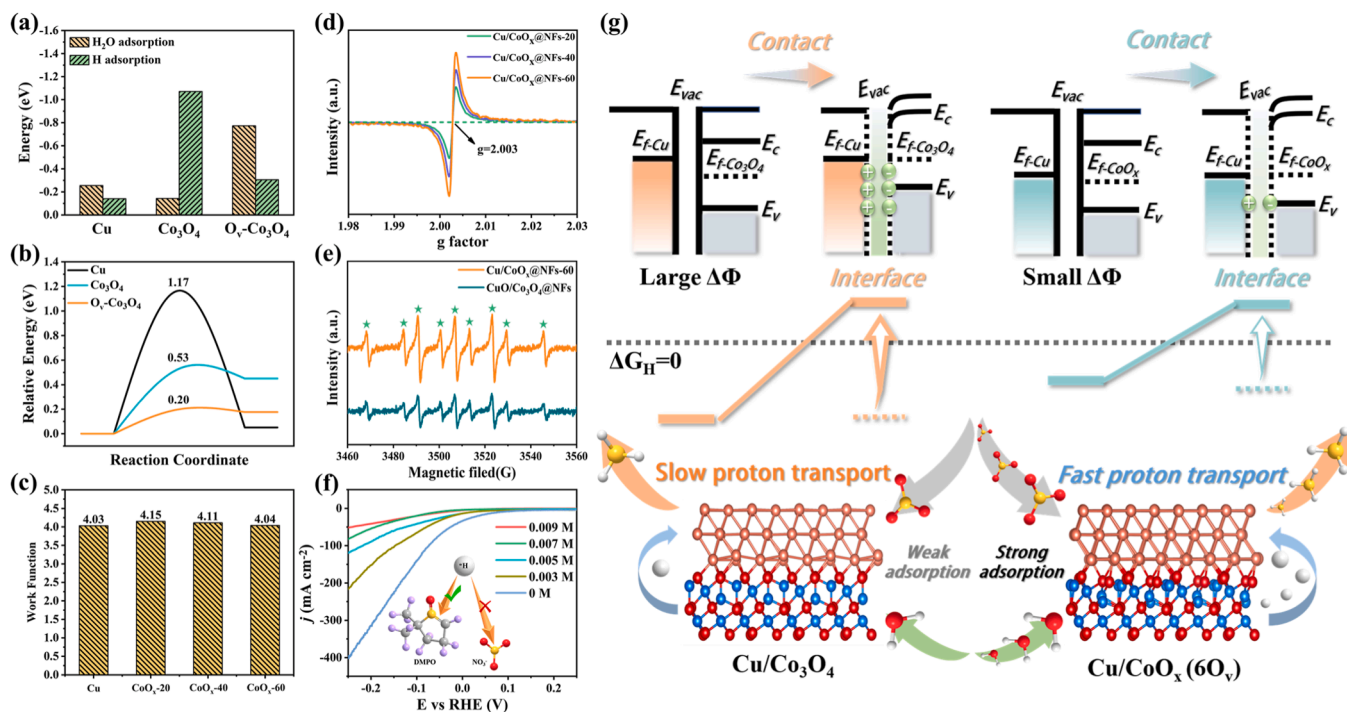**Fig. 4.** (a) Calculated H_2O adsorption energies and H adsorption free energies on Cu, Co_3O_4, and Co_3O_4 with 6 O_v (O_v-Co_3O_4), where more negative values mean stronger binding strength. (b) Minimum energy pathway for water dissociation on Cu, Co_3O_4, and O_v-Co_3O_4. (c) Work functions of Cu, CoO_x-20, CoO_x-40, and CoO_x-60 obtained from the UPS tests. (d) EPR spectra of Cu/CoO_x @NFs-20, Cu/CoO_x @NFs-40, and Cu/CoO_x @NFs-60. (e) EPR spectra of the solutions obtained after 5 min of the NO_3^-RR electrocatalyzed by the Cu/CoO_x @NF-60 and CuO/Co_3O_4 @NFs samples in 1 M KOH under argon using DMPO as the *H-trapping reagent. (f) Effect of different DMPO concentrations on the NO_3^-RR performance of Cu/CoO_x @NF-60. (g) Schematic representation of the effect of $\Delta\Phi$ on the electronic configuration and hydrogen spillover phenomenon at the heterogeneous interface in the Cu/CoO_x @NFs electrocatalysts and the corresponding mechanistic insights. E_{vac} = vacuum energy, E_c = conduction band, E_v = valence band, and E_f = Fermi level.

of the O_v-rich Cu/CoO$_x$ heterogeneous interfacial structures and theoretically determined the process of *H generation and transfer between the heterogeneous structures. First, surface configurations of water adsorbed on the Cu, Co$_3$O$_4$ (pristine), and Co$_3$O$_4$ (6 O_v) structural models were constructed and optimized individually (Figs. S21–S24). Thereafter, the adsorption energy and water dissociation potential barriers of the three structural models were investigated using DFT calculations (Figs. 4(a) and 4(b)). The results showed that the presence of O_v significantly increased the adsorption intensity of the Co$_3$O$_4$ (6 O_v) structure on water, and the adsorption energy of water on the Co$_3$O$_4$ (6 O_v) structure (−0.77 eV) was much larger than that on Cu and Co$_3$O$_4$ (−0.25 eV and −0.14 eV, respectively) (Fig. 1(b)). Additionally, the presence of O_v was able to promote the dissociation of water from the Co$_3$O$_4$ (6 O_v) structure. Compared to 1.17 eV (Cu) and 0.53 eV (Co$_3$O$_4$), the smaller hydrolytic separation barrier (0.20 eV) also indicates that the water adsorbed on the Co$_3$O$_4$ (6 O_v) structure was more inclined to dissociate to form *H. In other words, the above results confirmed that *H is more likely to be produced on oxygen-rich defective Co$_3$O$_4$ (6 O_v) structures. Additionally, the *H adsorption energies of the Cu, Co$_3$O$_4$ (pristine), and Co$_3$O$_4$ (6 O_v) structural models were calculated (Fig. 4 (a)) to investigate the potential NO$_3^-$RR active sites and the transfer and enrichment of *H on the heterogeneous interfacial structures. The results revealed that the *H adsorption energies of the Co$_3$O$_4$ (pristine) and O_v-Co$_3$O$_4$ (6 O_v) structures were −1.07 eV and −0.30 eV, respectively. However, *H diffused more easily on the surface of the Co$_3$O$_4$ (6 O_v) structures. Generally, the addition of O_v made it easy for Co$_3$O$_4$ (6 O_v) to dissociate water molecules to generate *H. This substantial difference in the ability to adsorb *H resulted in an overflow of *H from the O_v-Co$_3$O$_4$ (6 O_v) surface to the Cu surface, enhancing the degree of hydrogen coverage on the Cu surface. Next, the effects of Cu on the NO$_3^-$ adsorption properties of four heterogeneous structural models, namely, Cu/Co$_3$O$_4$ (pristine), Cu/Co$_3$O$_4$ (3 O_v), Cu/Co$_3$O$_4$ (6 O_v), and Cu/Co$_3$O$_4$ (9 O_v), were investigated using DFT calculations. Furthermore, an investigation was conducted to assess the impact of O_v on the adsorption of NO$_3^-$ at the primary Cu active site when the heterogeneous interfacial structure exhibited synergistic functionality. The results were shown in Figs. S25 and S26. Cu in the Cu/Co$_3$O$_4$ (6 O_v) model had the strongest adsorption energy for NO$_3^-$ relative to Cu in the other models. This finding is not only consistent with a previous finding [58], but it also further validates the positive contribution of O_v to the synergistic effects of the Cu/CoO$_x$ heterogeneous interfacial structure.

Considering the important contribution of *H to the electrocatalytic reduction reaction, we attempted to experimentally verify the beneficial effect of *H on the NO$_3^-$RR kinetics. First, we verified the presence of *H in the reaction system. The ability of the reconstituted Cu/CoO$_x$ @NFs active electrocatalyst to promote *H generation was investigated and verified using electrochemical in situ EPR spectroscopy with 5,5-dimethyl-1-pyrroline-N-oxide (DMPO) as the trapping agent. The test was performed in 1 M KOH to exclude possible interferences. The results were shown in Fig. 4(e), and nine EPR peaks belonging to DMPO-H* can be observed. The Cu/CoO$_x$ @NFs had a stronger EPR peak than the CuO/Co$_3$O$_4$ @NFs during the same negative potential, confirming that the Cu/CoO$_x$ @NFs samples were more conducive to *H formation. These results confirmed that O_v can promote *H generation, effectively accelerating the NO$_3^-$RR kinetics, which was consistent with the DFT calculation results. DMPO was directly used as an *H scavenger in the Cu/CoO$_x$ @NFs electrocatalytic process for the NO$_3^-$RR to directly investigate the actual effect of *H on the NO$_3^-$RR. Different DMPO concentrations were configured separately and added to the NO$_3^-$RR test system within the same test interval range. As shown in Fig. 4(f), the LSV curves were recorded after the addition of different DMPO concentrations. The result revealed that the test current density decreased sharply as *H was consumed by the different DMPO concentrations. The quenching effect of DMPO on *H reduced its participation in the NO$_3^-$RR, significantly decreasing its NO$_3^-$RR performance. The above results clearly indicated the strong correlation between *H and the

kinetic process of the NO$_3^-$RR. They also confirmed that the synergistic effect of Cu/CoO$_x$ heterogeneous interfacial structures substantially promotes the NO$_3^-$RR.

The magnitude of the $\Delta\Phi$ value between Cu and CoO$_x$ and its influence on the NO$_3^-$RR performance were mainly manifested in how the $\Delta\Phi$ affects and induces charge accumulation and rearrangement at the heterogeneous interface (Fig. 4(g)). Two heterogeneous interfacial systems, Cu/Co$_3$O$_4$ and Cu/CoO$_x$, were compared. The introduction of O_v inhibited the movement of interfacial charges and reduced the accumulation of charges at the interface. These manifestations significantly reduced the energy barrier to allow *H to cross the interface, thermodynamically promoting the overflow of *H at the interface. In addition, a small $\Delta\Phi$ value induced a charge rearrangement, forming electron-rich regions at the Cu and CoO$_x$ phases rather than at the heterogeneous interface. This property strengthened the ability of CoO$_x$ to adsorbed and dissociated water and weakened its ability to adsorb *H. This influence also enhanced the adsorption of Cu on NO$_3^-$. Eventually, the overflow of *H onto the Cu surface also promoted the NO$_3^-$RR. These results clarified that Cu/CoO$_x$ heterogeneous interfacial structures with small $\Delta\Phi$ values could exhibit strong synergistic effects. These properties coincide with our basic view on the design of electroreduction catalysts with rich heterogeneous interfacial structures. Both the experimental and theoretical calculations confirmed the important concept that advanced electrochemical reduction catalysts could be constructed by rationally designing $\Delta\Phi$, which was the key parameter.

We reveal how $\Delta\Phi$ affects the synergistic effect of O_v-rich Cu/CoO$_x$ heterogeneous interfacial structures to enhanced their NO$_3^-$RR performance. (i) The O_v could modulate the $\Delta\Phi$ value of the heterogeneous interfacial structure; (ii) $\Delta\Phi$ was a key factor affecting the synergistic effect of heterogeneous interfacial structures; (iii) A small $\Delta\Phi$ between heterogeneous interfacial structures could promoted electron rearrangement at the Cu and CoO$_x$ interfaces, effectively promote *H production on CoO$_x$, and enhance the adsorption of the reactants on Cu; (iv) Additional *H spills over from the CoO$_x$ surface to the Cu surface, enhancing the degree of hydrogen coverage on the Cu surface, which consequently enhanced the NO$_3^-$RR performance. The experimental results and DFT calculations confirmed that a suitable O_v concentration, a small $\Delta\Phi$ value, and an optimized electronic structure were the three main factors contributing to the excellent NO$_3^-$RR catalytic activity of Cu/CoO$_x$ @NFs. This work not only provides a new concept of rationally designing and precisely controlling heterogeneous structure-based electrocatalysts but also provides a new effective method for exploring the mechanism of heterogeneous engineering and O_v engineering to jointly regulate electrocatalytic reduction.

4. Conclusion

In this study, we investigated and confirmed that a suitable $\Delta\Phi$ between the Cu/CoO$_x$ heterointerfaces could enhance the synergistic effects and improves their electrocatalytic activity. Both the experimental and DFT calculations revealed that the introduction of O_v on CoO$_x$ could efficiently modulate the $\Delta\Phi$ between Cu/CoO$_x$, thereby controlling the interfacial electron transfer from Cu to CoO$_x$, enhanced the adsorption and reduced reduction reaction energy barrier of Cu to nitrate. Moreover, CoO$_x$ containing moderate O_v concentrations had strong water dissociation ability to produce *H, and then the *H spilled over onto the Cu surface at cathodic potential, significantly increasing hydrogen coverage on the Cu surface. The strong adsorption properties of Cu for reactants combined with abundant *H can greatly promote the NO$_3^-$RR. The Cu/CoO$_x$ @NFs exhibited excellent ability for the electrocatalytic reduction of NO$_3^-$ to produce NH$_3$ owing to the powerful synergistic effects of their heterogeneous interfaces as well as their structural properties. The FE$_{NH3}$ and current density of the Cu/CoO$_x$ @NFs were as high as 95.1% and 400 mA cm^{-2}, respectively, at a low reaction potential of −0.15 V$_{RHE}$. This work provides new reference ideas and evidence for efficient proton-coupled electron reduction reactions and

mechanistic research by adjusting $\Delta\Phi$ to rationally design heterogeneous interfaces.

CRediT authorship contribution statement

Chao Feng, Weiliang Zhou, Hanyang Wu, Qihua Huo, Jiaxin Shao, Xuan Li: Carried out the synthesis, materials characterizations, and electrochemical measurements. **Chao Feng, Qi Hu:** Designed the experiments and wrote the manuscript. **Hengpan Yang, Qi Hu, Chuanxin He:** Conceived the project and ideal.

Declaration of Competing Interest

The authors declare that they have no known competing financial interests or personal relationships that could have appeared to influence the work reported in this paper.

Data availability

Data will be made available on request.

Appendix A. Supporting information

Supplementary data associated with this article can be found in the online version at doi:10.1016/j.apcatb.2023.123280.

References

[1] J. Chen, C. Chen, M. Qin, B. Li, B. Lin, Q. Mao, H. Yang, B. Liu, Y. Wang, Reversible hydrogen spillover in Ru-WO$_{3-x}$ enhances hydrogen evolution activity in neutral pH water splitting, Nat. Commun. 13 (2022) 5382.

[2] B. Wulan, X. Cao, D. Tan, J. Ma, J. Zhang, To stabilize oxygen on In/In$_2$O$_3$ heterostructure via joule heating for efficient electrocatalytic CO$_2$ reduction, Adv. Funct. Mater. 33 (2022), 2209114.

[3] Q. Qian, J. Zhang, J. Li, Y. Li, X. Jin, Y. Zhu, Y. Liu, Z. Li, A. El-Harairy, C. Xiao, G. Zhang, Y. Xie, Artificial heterointerfaces achieve delicate reaction kinetics towards hydrogen evolution and hydrazine oxidation catalysis, Angew. Chem. Int. Ed. 60 (2021) 5984–5993.

[4] L. Zhao, Y. Zhang, Z. Zhao, Q.H. Zhang, L.B. Huang, L. Gu, G. Lu, J.S. Hu, L.J. Wan, Steering elementary steps towards efficient alkaline hydrogen evolution via size-dependent Ni/NiO nanoscale heterosurfaces, Natl. Sci. Rev. 7 (2020) 27–36.

[5] J. Zhou, F. Pan, Q. Yao, Y. Zhu, H. Ma, J. Niu, J. Xie, Achieving efficient and stable electrochemical nitrate removal by in-situ reconstruction of Cu$_2$O/Cu electroactive nanocatalysts on Cu foam, Appl. Catal. B: Environ. 317 (2022), 121811.

[6] J. Liu, S. Duan, H. Shi, T. Wang, X. Yang, Y. Huang, G. Wu, Q. Li, Rationally designing efficient electrocatalysts for direct seawater splitting: Challenges, achievements, and promises, Angew. Chem. Int. Ed. 61 (2022), e202210753.

[7] L. He, T. Zeng, F. Yao, Y. Zhong, C. Tan, Z. Pi, K. Hou, S. Chen, X. Li, Q. Yang, Electrocatalytic reduction of nitrate by carbon encapsulated Cu-Fe electroactive nanocatalysts on Ni foam, J. Colloid Interface Sci. 634 (2023) 440–449.

[8] L. He, F. Yao, Y. Zhong, C. Tan, K. Hou, Z. Pi, S. Chen, X. Li, Q. Yang, Achieving high-performance electrocatalytic reduction of nitrate by N-rich carbon-encapsulated Ni-Cu bimetallic nanoparticles supported nickel foam electrode, J. Hazard. Mater. 436 (2022), 129253.

[9] W. He, J. Zhang, S. Dieckhöfer, S. Varhade, A.C. Brix, A. Lielpetere, S. Seisel, J.R. C. Junqueira, W. Schuhmann, Splicing the active phases of copper/cobalt-based catalysts achieves high-rate tandem electroreduction of nitrate to ammonia, Nat. Commun. 13 (2022) 1129.

[10] D. Chen, R. Lu, R. Yu, Y. Dai, H. Zhao, D. Wu, P. Wang, J. Zhu, Z. Pu, L. Chen, J. Yu, S. Mu, Work-function-induced interfacial built-in electric fields in Os-OsSe$_2$ heterostructures for active acidic and alkaline hydrogen evolution, Angew. Chem. Int. Ed. 61 (2022), e202208642.

[11] S.-Q. Liu, M.-R. Gao, S. Liu, J.-L. Luo, Hierarchically assembling cobalt/nickel carbonate hydroxide on copper nitride nanowires for highly efficient water splitting, Appl. Catal. B: Environ. 292 (2021), 120148.

[12] S.-Q. Liu, M.-R. Gao, S. Liu, J.-L. Luo, Hierarchically assembling cobalt/nickel carbonate hydroxide on copper nitride nanowires for highly efficient water splitting, Appl. Catal. B: Environ. 292 (2021), 120148.

[13] C. Feng, Y. Guo, S. Qiao, Y. Xie, L. Zhang, L. Zhang, W. Wang, J. Wang, 2-Methylimidazole as a nitrogen source assisted synthesis of a nano-rodshaped Fe/FeN@N-C catalyst with plentiful FeN active sites and enhanced ORR activity, Appl. Surf. Sci. 533 (2020), 147481.

[14] S. Zhou, Y. Zhao, R. Shi, Y. Wang, A. Ashok, F. Heraly, T. Zhang, J. Yuan, Vacancy-rich MXene-immobilized Ni single atoms as a high-performance electrocatalyst for the hydrazine oxidation reaction, Adv. Mater. 34 (2022), e2204388.

[15] H. Du, H. Guo, K. Wang, X. Du, B.A. Beshiwork, S. Sun, Y. Luo, Q. Liu, T. Li, X. Sun, Durable electrocatalytic reduction of nitrate to ammonia over defective pseudobrookite Fe$_2$TiO$_5$ nanofibers with abundant oxygen vacancies, Angew. Chem. Int. Ed. 62 (2023) e202215782.

[16] Z. Zhuang, Y. Li, Z. Li, F. Lv, Z. Lang, K. Zhao, L. Zhou, L. Moskaleva, S. Guo, L. Mai, MoB/g-C$_3$N$_4$ interface materials as a schottky catalyst to boost hydrogen evolution, Angew. Chem. Int. Ed. 57 (2018) 496–500.

[17] W. Gao, J.V. Perales-Rondon, J. Michalička, M. Pumera, Ultrathin manganese oxides enhance the electrocatalytic properties of 3D printed carbon catalysts for electrochemical nitrate reduction to ammonia, Appl. Catal. B: Environ. 330 (2023), 122632.

[18] C. Feng, Y. Guo, Y. Xie, X. Cao, S. Li, L. Zhang, W. Wang, J. Wang, Bamboo-like nitrogen-doped porous carbon nanofibers encapsulated nickel-cobalt alloy nanoparticles composite material derived from the electrospun fiber of a bimetal-organic framework as efficient bifunctional oxygen electrocatalysts, Nanoscale 12 (2020) 5942–5952.

[19] F. Yao, F. Jia, Q. Yang, F. Chen, Y. Zhong, S. Chen, L. He, Z. Pi, K. Hou, D. Wang, X. Li, Highly selective electrochemical nitrate reduction using copper phosphide self-supported copper foam electrode: Performance, mechanism, and application, Water Res 193 (2021), 116881.

[20] F. Yao, Q. Yang, Y. Zhong, X. Shu, F. Chen, J. Sun, Y. Ma, Z. Fu, D. Wang, X. Li, Indirect electrochemical reduction of nitrate in water using zero-valent titanium anode: Factors, kinetics, and mechanism, Water Res 157 (2019) 191–200.

[21] C. Feng, Y. Xie, S. Qiao, Y. Guo, S. Li, L. Zhang, W. Wang, J. Wang, Porous MoWN/MoWC@NAC nano-octahedrons synthesized via confined carburization and vapor deposition in MOFs as efficient trifunctional electrocatalysts for oxygen reversible catalysis and hydrogen production in the same electrolyte, J. Colloid Interface Sci. 601 (2021) 626–639.

[22] D. Xu, S.N. Zhang, J.S. Chen, X.H. Li, Design of the synergistic rectifying interfaces in Mott–Schottky catalysts, Chem. Rev. 123 (2023) 1–30.

[23] Q. Hu, Z. Wang, X. Huang, Y. Qin, H. Yang, X. Ren, Q. Zhang, J. Liu, C. He, A unique space confined strategy to construct defective metal oxides within porous nanofibers for electrocatalysis, Energ. Environ. Sci. 13 (2020) 5097–5103.

[24] Y. Shi, Z.R. Ma, Y.Y. Xiao, Y.C. Yin, W.M. Huang, Z.C. Huang, Y.Z. Zheng, F.Y. Mu, R. Huang, G.Y. Shi, Y.Y. Sun, X.H. Xia, W. Chen, Electronic metal-support interaction modulates single-atom platinum catalysis for hydrogen evolution reaction, Nat. Commun. 12 (2021) 3021.

[25] S. Zhou, H. Jang, Q. Qin, L. Hou, M.G. Kim, S. Liu, X. Liu, J. Cho, Boosting hydrogen evolution reaction by phase engineering and phosphorus doping on Ru/P-TiO$_2$, Angew. Chem. Int. Ed. 61 (2022), e202212196.

[26] L. Zhai, X. She, L. Zhuang, Y. Li, R. Ding, X. Guo, Y. Zhang, Y. Zhu, K. Xu, H.J. Fan, S.P. Lau, Modulating built-in electric field via variable oxygen affinity for robust hydrogen evolution reaction in neutral media, Angew. Chem. Int. Ed. 61 (2022), e202116057.

[27] K. Ji, M. Xu, S.M. Xu, Y. Wang, R. Ge, X. Hu, X. Sun, H. Duan, Electrocatalytic hydrogenation of 5-hydroxymethylfurfural promoted by a Ru1Cu single-atom alloy catalyst, Angew. Chem. Int. Ed. 61 (2022), e202209849.

[28] J. Li, G. Zhan, J. Yang, F. Quan, C. Mao, Y. Liu, B. Wang, F. Lei, L. Li, A.W.M. Chan, L. Xu, Y. Shi, Y. Du, W. Hao, P.K. Wong, J. Wang, S.X. Dou, L. Zhang, J.C. Yu, Efficient ammonia electrosynthesis from nitrate on strained ruthenium nanoclusters, J. Am. Chem. Soc. 142 (2020) 7036–7046.

[29] N. Wang, P. Ou, S.F. Hung, J.E. Huang, A. Ozden, J. Abed, I. Grigioni, C. Chen, R. K. Miao, Y. Yan, J. Zhang, Z. Wang, R. Dorakhan, A. Badreldin, A. Abdel-Wahab, D. Sinton, Y. Liu, H. Liang, E.H. Sargent, Strong-proton-adsorption Co-based electrocatalysts achieve active and stable neutral seawater splitting, Adv. Mater. 35 (2023), e2210057.

[30] Y. Tan, Y. Zhu, X. Cao, Y. Liu, J. Li, Z. Chen, J. Hu, Discovery of hydrogen spillover-based binary electrocatalysts for hydrogen evolution: From theory to experiment, ACS Catal. 12 (2022) 11821–11829.

[31] C. Mao, J. Wang, Y. Zou, G. Qi, J.Y. Yang Loh, T. Zhang, M. Xia, J. Xu, F. Deng, M. Ghoussoub, N.P. Kherani, L. Wang, H. Shang, M. Li, J. Li, X. Liu, Z. Ai, G. A. Ozin, J. Zhao, L. Zhang, Hydrogen spillover to oxygen vacancy of TiO$_{2-x}$H$_y$/Fe: breaking the scaling relationship of ammonia synthesis, J. Am. Chem. Soc. 142 (2020) 17403–17412.

[32] S. Xu, Y. Shi, Z. Wen, X. Liu, Y. Zhu, G. Liu, H. Gao, L. Sun, F. Li, Polystyrene spheres-templated mesoporous carbonous frameworks implanted with cobalt nanoparticles for highly efficient electrochemical nitrate reduction to ammonia, Appl. Catal. B: Environ. 323 (2023), 122192.

[33] L. Liu, T. Xiao, H. Fu, Z. Chen, X. Qu, S. Zheng, Construction and identification of highly active single-atom Fe1-NC catalytic site for electrocatalytic nitrate reduction, Appl. Catal. B: Environ. 323 (2023), 122181.

[34] Z.Y. Wu, M. Karamad, X. Yong, Q. Huang, D.A. Cullen, P. Zhu, C. Xia, Q. Xiao, M. Shakouri, F.Y. Chen, J.Y.T. Kim, Y. Xia, K. Heck, Y. Hu, M.S. Wong, Q. Li,

I. Gates, S. Siahrostami, H. Wang, Electrochemical ammonia synthesis via nitrate reduction on Fe single atom catalyst, Nat. Commun. 12 (2021) 2870.

[35] L. Han, X.Y. Yu, X.W. Lou, Formation of prussian-blue-analog nanocages via a direct etching method and their conversion into Ni-Co-mixed oxide for enhanced oxygen evolution, Adv. Mater. 28 (2016) 4601–4605.

[36] Y. Wang, A. Xu, Z. Wang, L. Huang, J. Li, F. Li, J. Wicks, M. Luo, D.H. Nam, C. S. Tan, Y. Ding, J. Wu, Y. Lum, C.T. Dinh, D. Sinton, G. Zheng, E.H. Sargent, Enhanced nitrate-to-ammonia activity on copper-nickel alloys via tuning of intermediate adsorption, J. Am. Chem. Soc. 142 (2020) 5702–5708.

[37] Y. Feng, H. Yang, Y. Zhang, X. Huang, L. Li, T. Cheng, Q. Shao, Te-doped Pd nanocrystal for electrochemical urea production by efficiently coupling carbon dioxide reduction with nitrite reduction, Nano Lett. 20 (2020) 8282–8289.

[38] M. George, K.S. Nagaraja, N. Balasubramanian, Spectrophotometric determination of hydrazine, Talanta 75 (2008) 27–31.

[39] G. Kresse, J. Furthmüller, Efficient iterative schemes for ab initio total-energy calculations using a plane-wave basis set, Phys. Rev. B 54 (1996) 11169–11186.

[40] G. Kresse, D. Joubert, From ultrasoft pseudopotentials to the projector augmented-wave method, Phys. Rev. B 59 (1999) 1758–1775.

[41] P.E. Blochl, Projector augmented-wave method, Phys. Rev. B 50 (1994) 17953–17979.

[42] J.P. Perdew, J.A. Chevary, S.H. Vosko, K.A. Jackson, M.R. Pederson, D.J. Singh, C. Fiolhais, Atoms, molecules, solids, and surfaces: Applications of the generalized gradient approximation for exchange and correlation, Phys. Rev. B 46 (1992) 6671–6687.

[43] John P. Perdew, Y. Wang, Accurate and simple analytic representation ofthe electron-gas correlation energy, Phys. Rev. B 45 (1992) 13244–13249.

[44] H.J.ónsson Graeme Henkelman, Improved tangent estimate in the nudged elastic band method for finding minimum energy paths and saddle points, J. Chem. Phys. 113 (2000) 9978–9985.

[45] G. Henkelman, B.P. Uberuaga, H. Jónsson, A climbing image nudged elastic band method for finding saddle points and minimum energy paths, J. Chem. Phys. 113 (2000) 9901–9904.

[46] T. Hu, C. Wang, M. Wang, C.M. Li, C. Guo, Theoretical insights into superior nitrate reduction to ammonia performance of copper catalysts, ACS Catal. 11 (2021) 14417–14427.

[47] Y. Wang, W. Zhou, R. Jia, Y. Yu, B. Zhang, Unveiling the activity origin of a copper-based electrocatalyst for selective nitrate reduction to ammonia, Angew. Chem. Int. Ed. 59 (2020) 5350–5354.

[48] L. Mi, Q. Huo, J. Cao, X. Chen, H. Yang, Q. Hu, C. He, Achieving synchronization of electrochemical production of ammonia from nitrate and ammonia capture by constructing a "Two-In-One" flow cell electrolyzer, Adv. Energy Mater. 12 (2022), 2202247.

[49] J. Yu, Y. Qin, X. Wang, H. Zheng, K. Gao, H. Yang, L. Xie, Q. Hu, C. He, Boosting electrochemical nitrate-ammonia conversion via organic ligands-tuned proton transfer, Nano Energy 103 (2022), 107705.

[50] J. Zhang, Q. Xu, J. Wang, Y. Li, H. Jiang, C. Li, Dual-defective Co₃O₄ nanoarrays enrich target intermediates and promise high-efficient overall water splitting, Chem. Eng. J. 424 (2021) 130328.

[51] W. Kang, R. Wei, H. Yin, D. Li, Z. Chen, Q. Huang, P. Zhang, H. Jing, X. Wang, C. Li, Unraveling sequential oxidation kinetics and determining roles of multi-cobalt active sites on Co₃O₄ catalyst for water oxidation, J. Am. Chem. Soc. 145 (2023) 3470–3477.

[52] X. Wei, X. Wen, Y. Liu, C. Chen, C. Xie, D. Wang, M. Qiu, N. He, P. Zhou, W. Chen, J. Cheng, H. Lin, J. Jia, X.Z. Fu, S. Wang, Oxygen vacancy-mediated selective C-N coupling toward electrocatalytic urea synthesis, J. Am. Chem. Soc. 144 (2022) 11530–11535.

[53] Y. Men, X. Su, P. Li, Y. Tan, C. Ge, S. Jia, L. Li, J. Wang, G. Cheng, L. Zhuang, S. Chen, W. Luo, Oxygen-inserted top-surface layers of Ni for boosting alkaline hydrogen oxidation electrocatalysis, J. Am. Chem. Soc. 144 (2022) 12661–12672.

[54] Q. Hu, K. Gao, X. Wang, H. Zheng, J. Cao, L. Mi, Q. Huo, H. Yang, J. Liu, C. He, Subnanometric Ru clusters with upshifted D band center improve performance for alkaline hydrogen evolution reaction, Nat. Commun. 13 (2022) 3958.

[55] Y. Xie, C. Feng, Y. Guo, A. Hassan, S. Li, Y. Zhang, J. Wang, Dimethylimidazole and dicyandiamide assisted synthesized rich-defect and highly dispersed CuCo-Nₓ anchored hollow graphite carbon nanocages as efficient trifunctional electrocatalyst in the same electrolyte, J. Power Sources 517 (2022), 230721.

[56] H. Jiang, R. Luo, Y. Li, W. Chen, Recent advances in solid-liquid-gas three-phase interfaces in electrocatalysis for energy conversion and storage, EcoMat 4 (2022), e12199.

[57] F. Zhang, J. Chen, G.G. Wallace, J. Yang, Engineering electrocatalytic fiber architectures, Prog. Mater. Sci. 133 (2023), 101069.

[58] Z. Gong, W. Zhong, Z. He, Q. Liu, H. Chen, D. Zhou, N. Zhang, X. Kang, Y. Chen, Regulating surface oxygen species on copper (I) oxides via plasma treatment for effective reduction of nitrate to ammonia, Appl. Catal. B: Environ. 305 (2022), 121021.

[59] Y. Cao, S. Yuan, L. Meng, Y. Wang, Y. Hai, S. Su, W. Ding, Z. Liu, X. Li, M. Luo, Recent advances in electrocatalytic nitrate reduction to ammonia: mechanism insight and catalyst design, ACS Sustain. Chem. Eng. 11 (2023) 7965–7985.

[60] W. Gao, J.V. Perales-Rondon, J. Michalička, M. Pumera, Ultrathin manganese oxides enhance the electrocatalytic properties of 3D printed carbon catalysts for electrochemical nitrate reduction to ammonia, Appl. Catal. B: Environ. 330 (2023), 122632.

[61] D. Liu, L. Qiao, S. Peng, H. Bai, C. Liu, W.F. Ip, K.H. Lo, H. Liu, K.W. Ng, S. Wang, X. Yang, H. Pan, Recent advances in electrocatalysts for efficient nitrate reduction to ammonia, Adv. Funct. Mater. (2023) e2303480.

[62] T. Xiang, Y. Liang, Y. Zeng, J. Deng, J. Yuan, W. Xiong, B. Song, C. Zhou, Y. Yang, Transition metal single-atom catalysts for the electrocatalytic nitrate reduction: mechanism, synthesis, characterization, application, and prospects, Small (2023) e2303732.

[63] J. Zhao, L. Liu, Y. Yang, D. Liu, X. Peng, S. Liang, L. Jiang, Insights into electrocatalytic nitrate reduction to ammonia via Cu-based bimetallic catalysts, ACS Sustain. Chem. Eng. 11 (2023) 2468–2475.

[64] W. Song, L. Yue, X. Fan, Y. Luo, B. Ying, S. Sun, D. Zheng, Q. Liu, M.S. Hamdy, X. Sun, Recent progress and strategies on the design of catalysts for electrochemical ammonia synthesis from nitrate reduction, Inorg. Chem. Front. 10 (2023) 3489–3514.

[65] X. Fu, X. Zhao, X. Hu, K. He, Y. Yu, T. Li, Q. Tu, X. Qian, Q. Yue, M.R. Wasielewski, Y. Kang, Alternative route for electrochemical ammonia synthesis by reduction of nitrate on copper nanosheets, Appl. Mater. Today 19 (2020), 100620.

[66] P. Li, Z. Jin, Z. Fang, G. Yu, A surface-strained and geometry-tailored nanoreactor that promotes ammonia electrosynthesis, Angew. Chem. Int. Ed. 59 (2020) 22610–22616.

[67] H. Xu, Y. Ma, J. Chen, W.X. Zhang, J. Yang, Electrocatalytic reduction of nitrate-a step towards a sustainable nitrogen cycle, Chem. Soc. Rev. 51 (2022) 2710–2758.